Pacific Northwest
NATIONAL LABORATORY

PNNL-34756

Survey Corrosion Testing Methodologies for Additively Manufactured Materials – PNNL

August 2023

Isabella van Rooyen
Thomas Hartmann
Vineet Joshi
Jonathan Wierschke

M4CT-23PN1306052

U.S. DEPARTMENT OF ENERGY

Prepared for the U.S. Department of Energy
under Contract DE-AC05-76RL01830

DISCLAIMER

PACIFIC NORTHWEST NATIONAL LABORATORY
operated by
BATTELLE
for the
UNITED STATES DEPARTMENT OF ENERGY
under Contract DE-AC05-76RL01830

Printed in the United States of America

Available to DOE and DOE contractors from
the Office of Scientific and Technical Information,
P.O. Box 62, Oak Ridge, TN 37831-0062
www.osti.gov
ph: (865) 576-8401
fox: (865) 576-5728
email: reports@osti.gov

Available to the public from the National Technical Information Service
5301 Shawnee Rd., Alexandria, VA 22312
ph: (800) 553-NTIS (6847)
or (703) 605-6000
email: info@ntis.gov
Online ordering: http://www.ntis.gov

PNNL-34756

Survey Corrosion Testing Methodologies for Additively Manufactured Materials – PNNL

August 2023

Isabella van Rooyen
Thomas Hartmann
Vineet Joshi
Jonathan Wierschke

Prepared for
the U.S. Department of Energy
under Contract DE-AC05-76RL01830

M4CT-23PN1306052

Pacific Northwest National Laboratory
Richland, Washington 99354

Summary

The Advanced Materials and Manufacturing Technology (AMMT) Program intends to develop cross-cutting technologies in support of a broad range of nuclear reactor technologies, and to maintain U.S. leadership in materials and manufacturing technologies for nuclear energy applications. The overarching vision of the AMMT Program is to accelerate the development, qualification, demonstration, and deployment of advanced materials and manufacturing technologies to enable reliable and economical nuclear energy.

This work is part of a multi-laboratory effort by Argonne National Laboratory, Idaho National Laboratory, and Pacific Northwest National Laboratory (PNNL) and is intended to support the objective of the AMMT Program by focusing on the corrosion performance of additively manufactured (AM) materials in nuclear reactor environments. Each laboratory is addressing in their individual reports, certain sections of a M3 level report due in September 2023. The collaborative M3 milestone will discuss the specific needs and considerations of corrosion testing for AM materials, including 316 stainless steels, for applications in nuclear reactors.

The aim of the collaborative work is a comprehensive review to understand the state-of-the-art of the field and to identify the research needs and strategies related to corrosion of AM materials for nuclear applications. The outcome of this work will help determine the basic needs and concerns specific to corrosion of AM materials for structural applications in reactor conditions and support future AMMT Program efforts for determining the corrosion responses of new AM materials for reactor environments.

Specifically, this PNNL report addresses through a literature survey specific topical areas of the future M3 milestone report, namely: (1) engineering concerns about corrosion behavior (limited to austenitic stainless steel), (2) key factors likely to influence corrosion properties of AM materials, (3) experimental capabilities needed for corrosion research on AM 316L (with specific focus on the available facilities at PNNL), and (4) a suggested path forward for AMMT Program's corrosion activity.

The literature survey revealed that no significant database or performance history exists for the corrosion behavior of additive manufacturing (AM) products, and no good comparative benchmark study exists for the different AM techniques. The limited corrosion experimental evaluations identified during the literature review showed a potential for the improved corrosion resistance of 316L materials. However, the effect of microstructure composition and corrosion seems not to be explored and is recommended for future work. No designated codes and standards for the corrosion testing of AM materials were identified, and no qualification/licensed precedent were found either.

Fabricated net-shaped AM components can have further additional benefits because the fabricated surface roughness reduces corrosion current densities, shifts corrosion potential in the positive (more noble) direction, and lowers corrosion rates. These need factors to be quantified for the different AM techniques and specifically in relation to the residual material stresses and microstructures.

Corrosion mechanistic studies do not seem be explored significantly and are highly recommended for future work. Such studies can be performed using modeling and experiment in concert. The capability and available facilities at PNNL provide a base for future experimental and modeling work related to corrosion mechanistic studies. Specifically, understanding the mechanistic pathways of reaction of different solutions associated with the underlying metal surface is highly critical. Earlier work by the authors used this approach to guide the experimental work to identify surface design strategies to reveal the underlying mechanisms and energetics. This type of modeling provided improved fundamental understanding of surface chemistry/corrosion behavior relationships, and these simulations can help identify the surface sites most vulnerable to specific species attack as well as establish which grains/chemical compositions/microstructures provide the best protection against such attacks. PNNL's corrosion facilities and capabilities include different length scale opportunities for further work and provide a diverse and complementary facility set for the participating AMMT program laboratories.

Finally, it is recommended that a complete Phenomena Identification and Ranking Table analysis be performed for each reactor type to fully comprehend the corrosion and other environmental challenges. This will ensure that the AMMT program is developing a corrosion strategy focused on application and therefore will provide the methodologies for future application of measures for a variety of material types.

Acknowledgments

The research presented here was supported by the Advanced Materials and Manufacturing Technology (AMMT) program of the U.S. Department of Energy (DOE) Office of Nuclear Energy. PNNL is a multi-program national laboratory operated for the DOE by Battelle Memorial Institute under Contract No. DE-AC05-76RL01830. The authors thank Dr. Ziqing Zhai for her initial contributions toward the development of the outline of the multi-laboratory collaborative milestone report.

Acronyms and Abbreviations

AFM	atomic force microscopy
AM	additively manufactured
AMMT	Advanced Materials and Manufacturing Technology
ANL	Argonne National Laboratory
BWR	boiling water reactor
DFT	density-functional theory
DOE	U.S. Department of Energy
EBSD	electron backscatter diffraction
EDS	energy dispersive X-ray spectroscopy
EIS	Electrochemical impedance spectroscopy
HIP	hot isostatic pressing
INL	Idaho National Laboratory
LMD	laser metal deposition
L-PBF	laser powder-bed fusion
OCP	open circuit potential
PD	potentiodynamic polarization
PIRT	Phenomena Identification and Ranking Table
PM	powder metallurgy
PNNL	Pacific Northwest National Laboratory
PWR	pressurized water reactor
SA	solution annealing
SCC	stress corrosion cracking
SCE	saturated calomel electrode
SECCIM	Scanning Electrochemical Cell Impedance Microscopy
SECCM	scanning electrochemical cell microscopy
SEM	scanning electron miscroscopy
SLM	selective laser melting
SS	stainless steel

Contents

Figures

Tables

1.0 Introduction

The U.S. Department of Energy's (DOE's) Advanced Materials and Manufacturing Technology Advanced Materials and Manufacturing Technology (AMMT) Program promotes the development of cross-cutting technologies in support of a broad range of nuclear reactor technologies, and to maintain U.S. leadership in materials and manufacturing technologies for nuclear energy applications. The overarching vision of the AMMT program is to accelerate the development, qualification, demonstration, and deployment of advanced materials and manufacturing technologies to enable reliable and economical nuclear energy.

The work reported here is part of a multi-laboratory effort by Argonne National Laboratory, (ANL), Idaho National Laboratory (INL), and Pacific Northwest National Laboratory (PNNL) to support the AMMT objective by focusing on the corrosion performance of additively manufactured (AM) materials in nuclear reactor environments. The respective work packages are led by INL and are as follows: (1) CT-23AN130602 – Survey corrosion testing methodologies for AM materials – ANL; (2) CT-23IN130604 – Survey corrosion testing methodologies for AM materials – INL; and (3) CT-23PN130605 – Survey corrosion testing methodologies for AM materials – PNNL.

ANL and PNNL will also each support the development of an additional M3 report (also called a white paper; see Figure 1) by providing technical input to INL via the respective M4 milestone reports under the three listed work packages above and contributing to the preparation and review of the M3 milestone report during September 2023. The collaborative white paper (M3 milestone) will discuss the specific needs and considerations of corrosion testing for AM materials, including 316 stainless steel (316 SS), for applications in nuclear reactors. Topics may include the different types of corrosion tests conducted in relevant reactor environments, characterizations at different length scales for general and localized corrosion, the effect of microstructure and manufacturing method on corrosion performance, the available testing methodologies and facilities, and any new testing methods required.

The collaborative work aims to provide a comprehensive review of AM corrosion behavior to understand the current state-of-the-art of the field and to identify the research needs and strategies related to corrosion of AM materials for nuclear applications. The objective is to develop a knowledge base of research activities and testing capabilities to characterize the environmental effects (specifically, corrosion effects) of AM materials. The outcome of this work will help determine the basic needs and concerns specific to the corrosion of AM materials for structural applications in reactor conditions and support future AMMT efforts for determining the corrosion responses of new AM materials for reactor environments.

Specifically, this PNNL report addresses through a literature survey specific topical areas of the future M3 milestone report, namely: (1) engineering concerns about corrosion behavior (limited to austenitic stainless steel), (2) key factors likely to influence corrosion properties of AM materials, (3) experimental capabilities needed for corrosion research on AM 316L (with specific focus on the available facilities at PNNL), and (4) a suggested path forward for AMMT Program's corrosion activity.

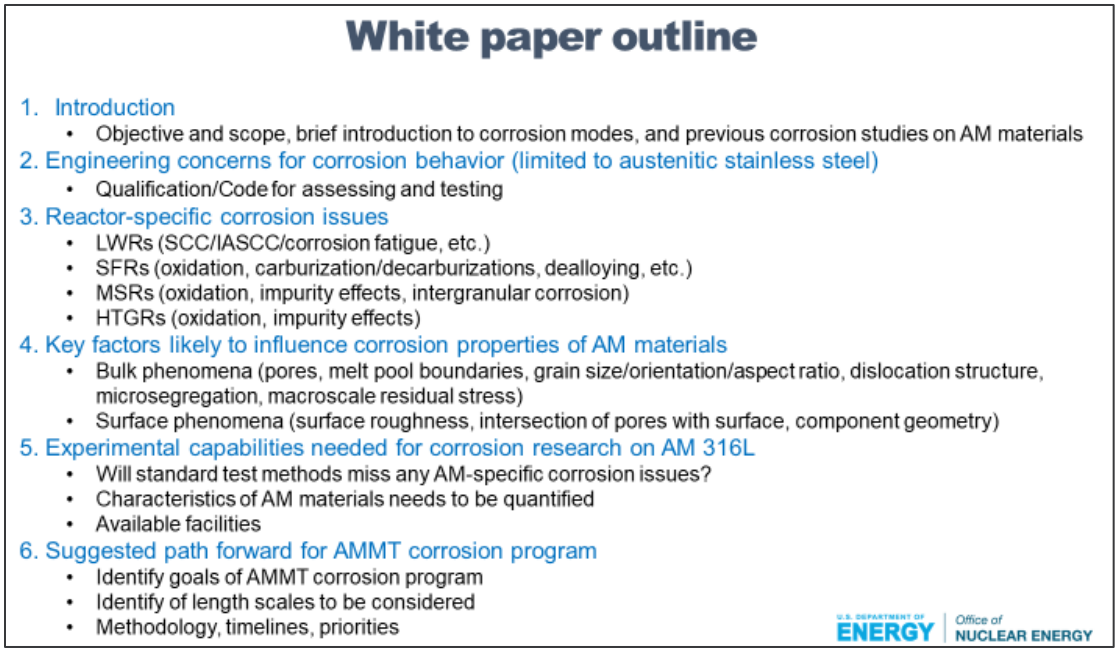

Figure 1. White paper (M3 milestone report) outline as prepared by the multi-national laboratory team of ANL, INL and PNNL (Jokisaari 2023).

2.0 Engineering Concerns for Corrosion Behavior (Limited to Austenitic Stainless Steel)

This section describes an overview of corrosion principles of austenitic stainless steels, the status of available codes and standards as well as the role of corrosion testing during qualification.

2.1 Corrosion of Austenitic Stainless Steels

Corrosion protection of stainless steel is based on the formation of a thin, passive film, composed primarily of iron/chromium oxides, that protects the underlying material from corrosion attacks. Other elements have been added to stainless steels to improve corrosion resistance in different environments. Elements such as Ni, Mn, Mo, W, and Cu have been shown to improve the corrosion resistance of stainless steels in different applications.

Although much work has been done to improve corrosion resistance, corrosion does still occur. Disruptions in the film create points for corrosion to begin. Disruptions may be caused by outside mechanical forces, such as scratching, or by localized stresses, such as dislocations along grain boundaries. Grain boundaries can also allow secondary phases to precipitate to the surface, creating a disruption in the passive film. Once the passive film has been interrupted, localized corrosion can begin. Ions in the surrounding medium allow for anodic reactions to corrode away localized regions of the steel. This is readily seen in pitting and crevice corrosion.

Localized corrosion can also occur along grain boundaries. In austenitic stainless steels, precipitation of chromium carbides near grain boundaries results in localized depletion of Cr concentration at the grain boundary. This reduces the passivation at the grain boundary and allows for intergranular attack.

The effectiveness of the passivation layer is also reduced by the presence of hydrogen. High concentrations of hydrogen can cause the structure and composition of the passivation layer to change. The presence of hydrogen also changes the electrochemical environment of the film and the base metal, reducing the stability of the passivation layer, heightening oxidation and dissolution kinetics, and promoting pitting and intergranular corrosion. High concentrations of hydrogen can reduce the hydrogen embrittlement is of particular concern to austenitic steels due to the higher Ni content.

2.2 Corrosion Codes and Standards

Evaluation of corrosion in materials is standardized in a series of ASTM procedures. ASTM G1 specifies the proper practices for preparing, cleaning, and evaluating corrosion specimens. ASTM G31 provides guidance for immersion testing. Procedures for testing intergranular corrosion of stainless steels are primarily described in ASTM A262 and A763. However, for nickel-rich alloys containing chromium, ASTM G28 is applicable.

Test methods for analyzing pitting corrosion in stainless steels are described in ASTM G48. Analysis of the results of pitting corrosion testing is governed by ASTM G46. An alternative method of investigating pitting in stainless steel is to measure the pitting potential electrochemically. The procedure for doing this is outlined in ASTM G150. The mechanisms

behind pitting and crevice corrosion are similar, so the testing procedures are similar and the same ASTM standards can be applied.

Stress corrosion cracking is a significant issue in steels, particularly in austenitic stainless steels. Stress corrosion cracking is a phenomenon that occurs in a material under stress. Understanding the stress corrosion cracking behavior of a material is important to understanding the long-term performance of the material. Investigation of stress corrosion cracking in steels is complex and is governed by many different standards. The testing required depends on the material and the environment. When investigating a new material, ASTM G129 is a good place to start because it evaluates how susceptible the material is to environmentally assisted cracking (ESC).

An alternative to standard submersion corrosion testing is electrochemical corrosion testing. ASTM G5 covers potentiodynamic anodic polarization measurements, while ASTM G59 covers potentiodynamic polarization resistance measurements. A more material-specific test standard is ASTM G61, which applies to potentiodynamic polarization measurements for Fe-, Ni-, and Co-based alloys. ASTM G3 sets the standard for representing the results of the electrochemical corrosion data, while ASTM G102 standardizes the methods for calculating corrosion rates and other information from the electrochemical tests.

2.3 Qualification/Regulation

Use of materials in nuclear power plants is heavily regulated. The environments to which the materials are exposed are some of the most extreme environments on Earth. Different components of the plants are subjected to different temperatures, pressures, flows, radiation fluxes, and chemical environments. For a material to be qualified for use in a particular application, the environment needs to be defined and testing must show that the material can reliably perform in that environment.

Testing to ASTM standards is important for qualifying the material for use in reactors. For in-reactor material, intergranular corrosion tends to be a significant issue. ASTM A262, *Standard Practices for Detecting Susceptibility to Intergranular Attack in Austenitic Stainless Steels*, is a standard test used to measure the degree of sensitization in reactor materials. That standard couples with ASTM G108, which describes the method of performing electrochemical potentiokinetic reactivation tests. The latter standard/This coupling provides a more quantitative method for measuring the degree of sensitization, though the test is written specifically for 304 and 304L stainless steel. No specific ASTM standards have been written for corrosion testing of materials produced through additive manufacturing.

The results of testing are used as part of the design basis for the licensing of nuclear power plants. The reactor designer needs to show that the material will be able to perform safely and reliably in its intended application. The design basis for nuclear power plants is given in Title 10 of the *Code of Federal Regulations* Part 50 (10 CFR Part 50) Appendix A: General Design Criteria for Nuclear Power Plants:

> Criterion 1—Quality standards and records. Structures, systems, and components important to safety shall be designed, fabricated, erected, and tested to quality standards commensurate with the importance of the safety functions to be

> performed. Where generally recognized codes and standards are used, they shall be identified and evaluated to determine their applicability, adequacy, and sufficiency and shall be supplemented or modified as necessary to assure a quality product in keeping with the required safety function. A quality assurance program shall be established and implemented to provide adequate assurance that these structures, systems, and components will satisfactorily perform their safety functions. Appropriate records of the design, fabrication, erection, and testing of structures, systems, and components important to safety shall be maintained by or under the control of the nuclear power unit licensee throughout the life of the unit.

The U.S. Nuclear Regulatory Commission oversees the licensing of nuclear power plants and reviews the proposed design. As part of their review, they consider the materials proposed for each application and determine whether the material has been sufficiently demonstrated to perform in such a manner that it can be reasonably ensured that all integrity criteria are met. Therefore, the developer or applicant needs to develop and compile an environmental effects evaluation through demonstration for regulatory approval.

3.0 Key Factors Likely to Influence the Corrosion Properties of AM Materials

Laser-based AM techniques, such as laser powder-bed fusion (LPBF), produce heterogeneous and anisotropic microstructures due to the layer-by-layer nature of the manufacturing process coupled with rapid solidification and large spatial thermal gradients. In L-PBF 316L, the intrinsic, multi-scale chemical heterogeneities (such as solute segregation, chromium depletion, and precipitate formation) inevitably alter the corrosion performance. Knowledge of these features and their dependence on the defect microstructure is therefore critical for understanding the corrosion properties of AM materials. In this section, literature data are compiled to eventually quantify the impact of microstructural bulk and surface phenomena on the corrosion properties of stainless-steel alloys produced by means of advanced manufacturing. To this end, some bulk phenomena such as porosity, melt pool boundaries, grainsizes and texture, dislocation structure, segregation, and residual stress are considered, as well as some surface phenomena such as surface roughness, intersection of pores with the surface, and design geometry. Overall, the strategy in revealing the improved corrosion resistance of design parts fabricated by AM methods is directly related to the precision to control fabrication parameters and the understanding of feedstock material properties.

3.1 Impact of Bulk Phenomena on AM Corrosion Properties

Material porosity, dislocation structure, build orientation, and microstructure all affect corrosion properties, as described in the ensuing sections.

3.1.1 Impact of Porosity

The metastable pitting characteristics of AM selective laser melting (SLM) 316L stainless steel (SS) of different porosities were compared with wrought 316L SS using potentiostatic testing (Sander et al. 2017), and the number of metastable pitting events were normalized to surface area and exposure time to obtain a metastable pit formation frequency (λ). These test results showed that the porosity of AM SLM 316L does affect the metastable pit formation frequency toward and pitting potentials E_{Pit} or breakdown potentials, while corrosion potentials are less affected, and corrosion current densities tend to be higher. With the variation of energy densities during fabrication, AM SLM 316L of different porosities have been produced (Sander et al. 2017) (Figure 2).

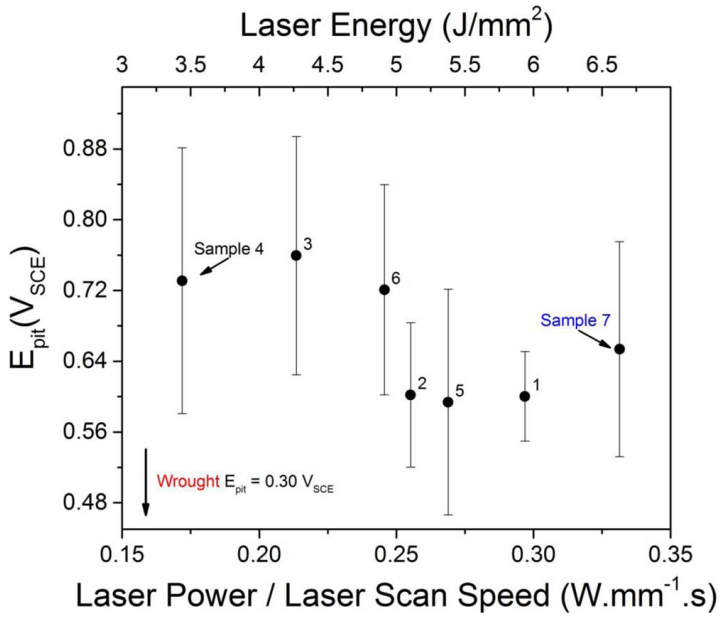

Figure 2. Pitting potential as a function of energy density, laser power/scan speed, and therefore porosity (Sander et al. 2017). Sample 4 represents the SLM samples exhibiting the highest porosity, while sample 7 represents the AM sample exhibiting the lowest porosity (highest density).

The measurement of pitting potentials of SLM 316L shows large standard deviations, which depletes quantitative statements. However, as an overall trend, the highest densities pitting potentials of SLM 316L are less noble but still improved relative to wrought SS316L. While the pitting potentials of SLM 316L are significantly more noble than those of wrought SS316L (Figure 3), the corrosion potentials do not show noticeable differences (Figure 4). Pitting potentials are defined by the potential at which protective passive coating (oxide layer) breaks down and the characteristic of the electrochemical system becomes transpassive. SLM 316L shows significant higher pitting potential than the wrought SS316L but very similar corrosion potentials. Furthermore, besides the improved porosity-derived pitting potentials of printed SLM 316L, their corrosion potentials do not show a clear trend with changing porosity and, as an important finding, their corrosion current densities are somewhat higher than those of the wrought counterparts. Overall, besides the repassivation potential (E_{rep}), which decreases with porosity, the values for pitting potential (E_{pit}), corrosion potential (E), and corrosion current density (i_{corr}) show no obvious trend as a function of achieved material density, and standard deviation of the collected data are too large to allow for quantitative statements.

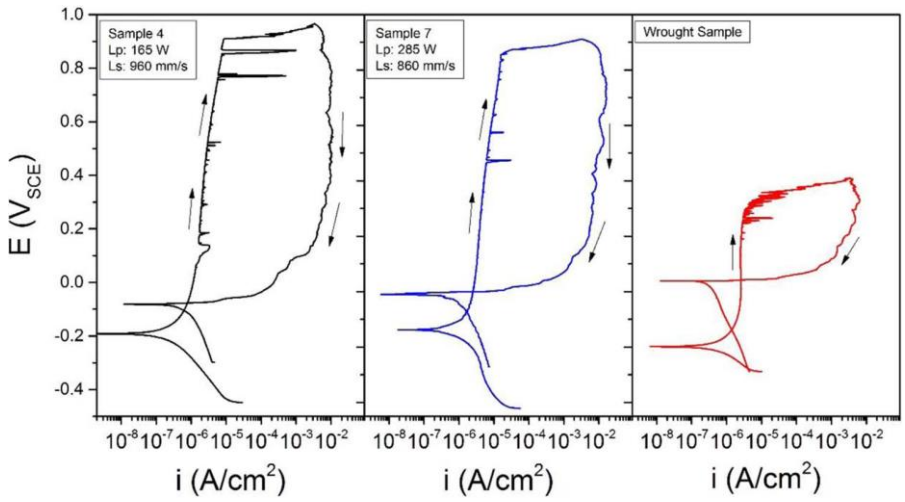

Figure 3. Polarization curves for SLM 316L specimens of highest (sample 4) and lowest (sample 7) porosities vs. wrought SS316L (Sander et al. 2017).

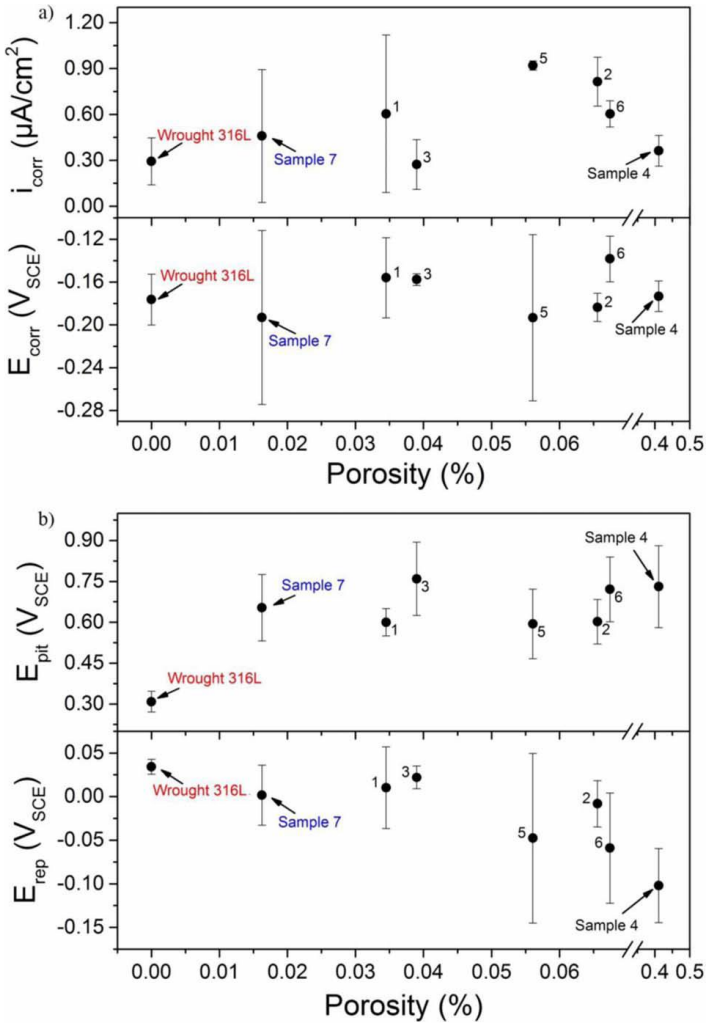

Figure 4. Corrosion potentials E_{corr}, corrosion current density i_{corr}, pitting potentials E_{pit}, and repassivation potential E_{rep} of SLM 316L vs. wrought SS316L (Sander et al. 2017).

3.1.2 Impact of Dislocation Structure on AM Corrosion Properties

Laser-based AM techniques, such as LPBF, produce heterogeneous and anisotropic microstructures due to the layer-by-layer nature of the manufacturing process coupled with rapid solidification and large spatial thermal gradients. In LPBF 316L, the intrinsic, multi-scale chemical heterogeneities such as solute segregation, chromium depletion and precipitate formation will inevitably alter the corrosion performance. Knowledge of these features and their dependence on the defect microstructure is therefore critical to understand corrosion properties of AM materials.

In the study by Sprouster et al. (2021), AM LPBF 316L specimen were produced at print speeds of 550-, 650-, and 700-mm s^{-1} and their corrosion potentials and corrosion current densities were measured in triplets. With increasing print speed, dislocation structures become more pronounced (Figure 5).

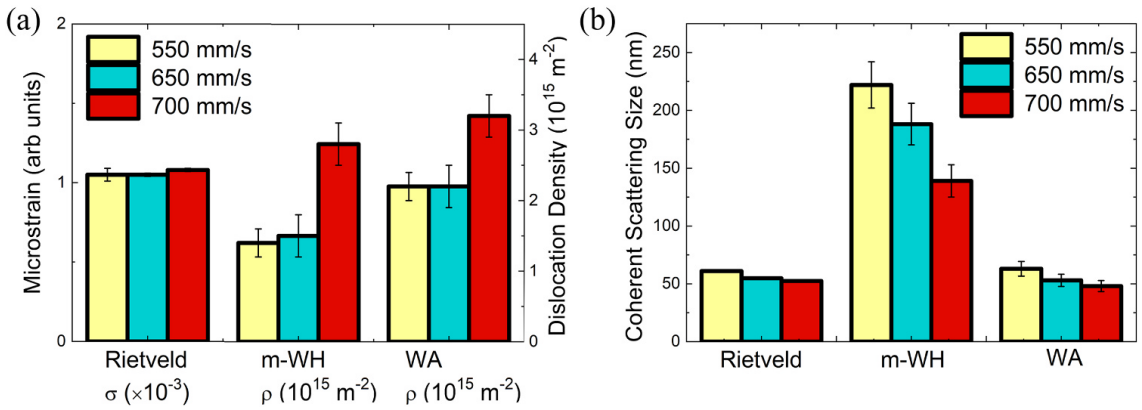

Figure 5. Quantitative structural characterization results as a function of printing speed from the Rietveld, modified Williamson-Hall (m-WH), and Warren-Averbach (WA) analyses including (a) microstrain, σ, and dislocation density, ρ, and (b) coherent scattering size (Sprouster et al. 2021).

An increase in printing speed from 550 mm s^{-1} to 700 mm s^{-1} promotes finer microstructures and a reduction in the coherent scattering size from 61 nm to 53 nm, increases the microstrain from 1.05 10^{-4} to 1.08 10^{-4}, and most importantly, increases dislocation densities from 1.5 10^{-15} m^{-2} to 2.8 10^{-15} m^{-2}. The reduction in scattering size toward higher print speed is accompanied by an increase in the dislocation density. Higher printing speeds promote enhanced solidification rates within a single print track to affect the solidification microstructure. Consistently, the largest lattice contraction/dislocation density and the smallest scattering sizes are reported for the specimens printed at 700 mm s^{-1} (Sprouster et al. 2021). The further reduction in lattice parameter is driven by dealloying and chromium depletion from the austenite matrix phase and resulting chromium segregation to the boundaries of the cellular microstructures.

The increased dislocation density induces some changes in corrosion potentials measured by cyclic voltammetry (Figure 6). Samples printed at higher speed show larger hysteresis eventually derived from disruption of the passive oxide film layer with subsequent stable pit growth, and hence an elevated anodic current until a repassivation conditions are reached (Sprouster et al.2021). However, corrosion potentials and pitting potentials move slightly to the more noble

region, but data scattering is too large to formulate a solid quantitative statement about how the dislocation structure impacts electrochemical potentials.

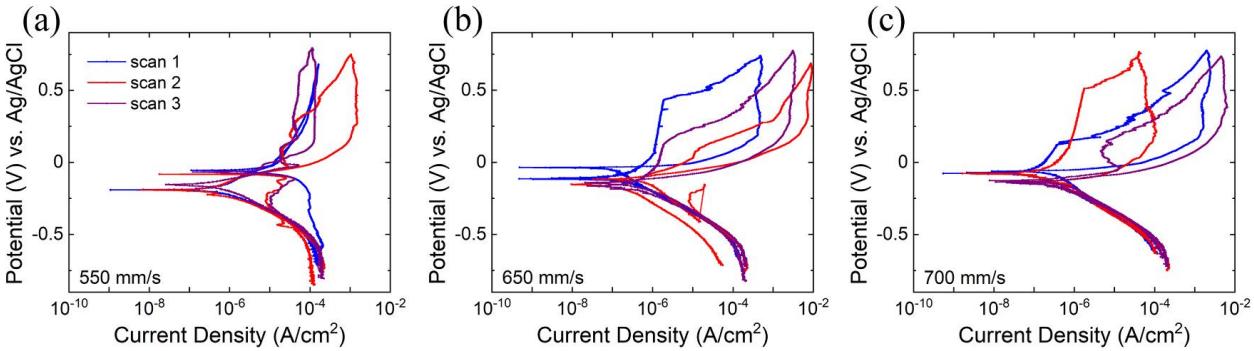

Figure 6. Cyclic voltammetry curves for polarization in a 3.5 percent NaCl solution on LPBF 316L printed at three speeds of (a) 550, (b) 650, and (c) 700 mm/s (Sprouster et al. 2021).

For now, it is fair to state that increasing the dislocation densities produces lower (less noble) corrosion potentials of L-PBF 316L and lower passivation current densities (Figure 7). Wrought SS316L shows corrosion potentials similar to the specimens produced at 650 mm s^{-1} combined with low passivation current densities like the 700 mm s^{-1} specimens. In the AM fabrication process, low print speed enables more noble corrosion potentials but far larger passivation current densities.

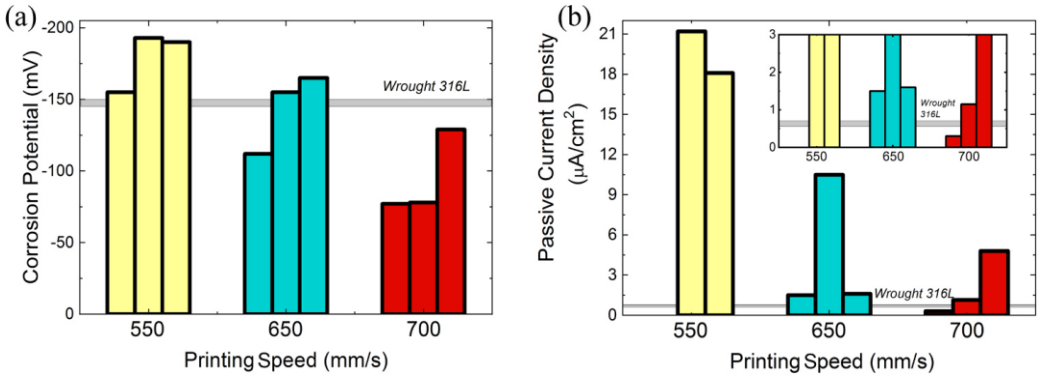

Figure 7. (a) Corrosion potential and (b) passive current density as a function of printing speed for the L-PBF 316L specimens. Measurement ranges for wrought 316L (grey bars) are included for reference with a magnified region around this range for the passive current density shown in the inset in (b) (Sprouster et al. 2021).

In the study by Sprouster et al. (2021), larger scan speeds and a more pronounced dislocation structure can lower pitting potential and increase the susceptibility for pitting corrosion compared with the wrought counterparts, but reverse effects are possible, as the 700 mm s-1 data in Figure 8 show. Overall, data scattering is large. The repassivation potentials of L-PBF 316L produced at low printing speed are lower than those of wrought SS316L, while at high printing speed and high defect densities the data scattering is too high for quantitative statements. It seems obvious that the reproducibility of dislocation structure at high scan speeds is low and data scattering is therefore high and diminishes the quality of any trend quantifications.

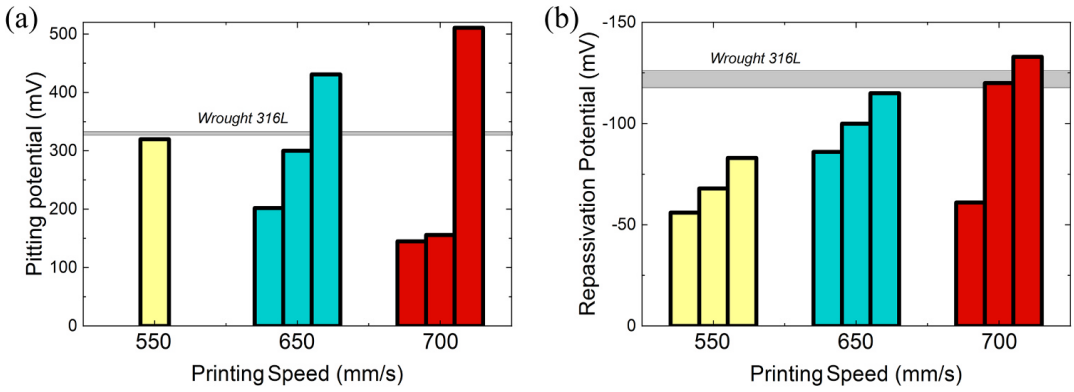

Figure 8. (a) Pitting and (b) repassivation potential measurements as a function of printing speed for the AM L-PBF 316L specimens. Measurement ranges for wrought 316L (grey rectangles) are included for reference (Sprouster et al. 2021).

3.1.3 Impact of Segregations on AM Corrosion Properties

Intergranular and intragranular Si- and Mn-rich oxide inclusions are present in laser AM austenitic stainless steel. The uniform oxide dispersions in AM materials promotes early initiation of microvoids and reduces materials' impact toughness relative to materials fabricated by powder metallurgy (hot isostatic pressing) and, more significantly, relative to wrought materials. For stress corrosion cracking in high-temperature water, the silica inclusions along the grain boundaries preferentially dissolve and appear to accelerate oxidation and cause extensive crack branching (Figure 9) (Lou et al. 2018).

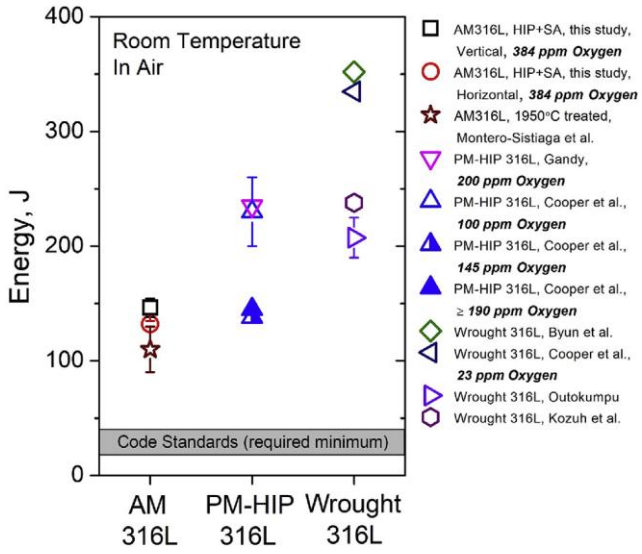

Figure 9. Comparison of Charpy impact toughness values at room temperature between AM 316L SS, powder metallurgy-hot isostatic pressing (PM-HIP) 316L SS, and wrought 316L SS. Data shown were obtained from solution-annealed materials that had coarse grain structures (Lou et al. 2018).

AM 316L SS was tested in two different orientations and showed, after full recrystallization, similar Charpy impact energies of about 130–150 J at room temperature, due to its equiaxed grain structures. The impact toughness of AM 316L produced by powder metallurgy and hipping, powder metallurgy-hot isostatic pressing (PM-HIP) 316L, decreases as the oxygen level increases. When oxygen concentration increased up to 190 ppm, the impact energy decreased from about 230 J to about 150 J, but no further decrease in impact toughness was observed for higher oxygen levels of above 200 ppm. By comparison, wrought products from forging generally show higher impact energy under the same testing conditions, and values above 200 J are generally reported, with highest impact energies of about 350 J (Lou et al. 2018). PM-HIP 316L SSformed from alloy powders generally exhibit impact energies between 200 and 250 J. In Figure 9, the impact energies of AM 316L SS and PM-HIP 316L SS are compared with that of wrought 316L SS. The latter contained only 23 ppm oxygen and showed superior fracture toughness, exhibiting an impact energy of 335 J.

Alloying metals such as manganese, molybdenum, and silicon have a strong affinity to oxygen and will form oxide particles to increase stress concentration and therefore reduce impact energies (Figure 10).

The higher oxygen concentrations of AM materials, relative to wrought alloys, are a result of adsorbed oxygen in the alloy feedstock powder. During manufacturing, micrometer-size oxides with Mn, Mo, or Si do form and adversely affect material properties. AM feed powder for producing structural material for nuclear deployment should undergo rigorous quality control to ensure as low as possible oxygen surface concentration, and suitable protocols must therefore be established.

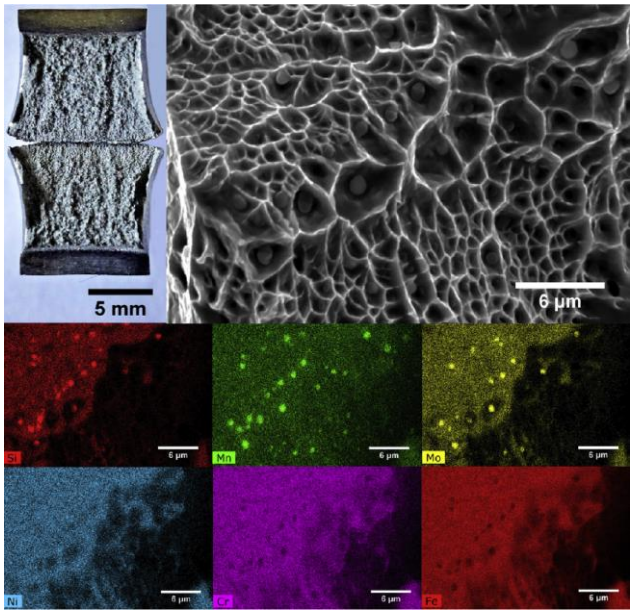

Figure 10. A scanning electron microscopy image and energy dispersive X-ray spectroscopy map of the Charpy impact fracture surface. All the spherical particles in the center of the dimples are oxides (Lou et al. 2018).

Silicon-rich oxide inclusions in AM 316L SS will reduce impact toughness and stress corrosion cracking (SCC) properties in high-temperature water relevant to nuclear technology. The intragranular oxide inclusions promote early microvoid formation to reduce the impact toughness relative to materials fabricated by PM-HIP and wrought materials, of comparable grain sizes (Lou et al. 2018). The reduced impact toughness is explained by the elevated oxygen level in the material and subsequently oxide particle formation. In high-temperature water, silicon-based oxide formation along the grain boundaries causes extensive crack branching and SCC. A higher volume fraction of oxide inclusions is expected to further reduce the impact toughness and increase the SCC susceptibility of AM materials in high-temperature water (Lou et al. 2018). The control of oxygen and high oxygen-affinity elements like Si during advanced manufacturing may help to reduce oxide formation. Further studies are needed to enhance the understanding of process-related oxide formation and its impact on the mechanical properties of AM structural material for nuclear deployment.

3.1.4 Impact of Build Orientation on AM Corrosion Properties

An experimental study by Lou et al. (2017) was conducted to provide improved understanding of the impact of the unique microstructural features of AM 316L SS on corrosion fatigue behavior in high-temperature water under boiling water reactor/pressurized water reactor (BWR/PWR)-type oxidizing conditions. In the study, AM LPBF 316L SS was heat treated to produce variations in microstructure and residual plastic strain, and the effects of crack propagation orientation were investigated. Three different heat treatment conditions were used to assess the effects of microstructure variations on the corrosion fatigue crack growth behavior: (1) stress relief at 650 °C for 2 h in argon, (2) HIP for 4 h at 1,150 °C and 100 MPa in argon, and (3) heat treatment at 955 °C for 4 h in argon. It was shown, that AM L-PBF 316L, after appropriate heat treatment, can exhibit corrosion fatigue crack growth response in high-temperature water similar to that of its wrought counterpart (Lou et al. 2017). However, hot isostatic pressing (HIP) treatment did not make a significant improvement over the stress-relieved condition regarding porosity. Solution annealing (SA; 955 °C for 4 h) was selected to produce a bimodal microstructure involving both recrystallized equiaxed grain and as-built characteristics. Full recrystallization, however, was not always achieved due to the strain variations at different locations of the as-built part and some un-recrystallized grains remained (Lou et al. 2017).

Samples show excellent reproducibility in crack propagation at 0.5 Hz and at 0.01 Hz. HIP and SA improved crack growth propagation by roughly 25–30 percent. AM 316L SS (Figure 11a) exhibited an anisotropic microstructure with an elongated solidification structure along the material building direction. Mixed grain boundaries from low to high angles were present in the material and formed a hierarchical order from submicron columnar structure to large dendrite grains. The columnar grains, generally showing low angle boundaries, and were mostly oriented toward the thermal gradient in build direction (Z direction). The average width of the columnar grain was around 300–500 nm (Lou et al. 2017). The heat treatment at 955 °C produced a partially recrystallized material (Figure 11b, Figure 13). In addition to high angle boundaries, annealing twins formed to compensate the energy released from the non-equilibrium microstructure developed during laser-based fabrication. In 316L SS, annealing twins are a preferable microstructure during recrystallization. In the un-recrystallized grains, the density of low angle boundaries was reduced due to defect annealing and the annihilation of dislocation cells (Lou et al. 2017).

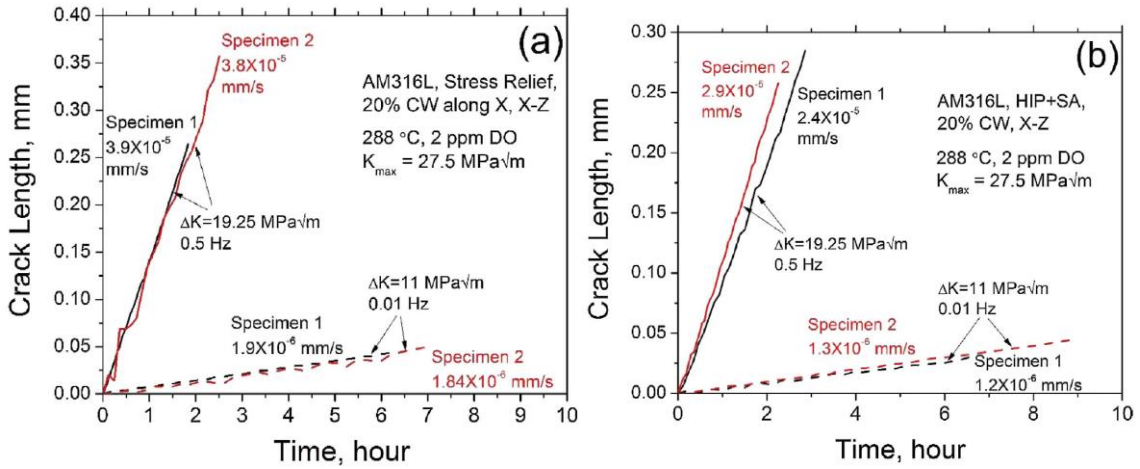

Figure 11. Corrosion fatigue crack growth at 0.5 and 0.01 Hz for (a) AM 316L SS, stress relief, plus 20 percent Cold Work (CW) perpendicular to build direction, along X, X-Z; (b) AM 316L SS, HIP + SA, plus 20 percent CW, X-Z (perpendicular to build direction) (Lou et al. 2017).

In Figure 12, a comparison of corrosion fatigue crack growth rates between the stress-relieved and recrystallized AM L-PBF 316L in 288 °C pure water containing 2 ppm dissolved oxygen (DO) is provided. In this example, maximum stress intensity K_{max} was kept at 27.5 MPa√m under a load frequency of 0.5 Hz. As a result of the grain structure, stress-relieved AM 316L SS exhibited a far higher crack propagation rate along the material building direction (X-Z) than along the normal to the material building direction (Z-X). The AM 316L SS after HIP + SA exhibited improved performance and a fairly similar crack propagation rate than the Z-X oriented stress-relieved material. Notice that HIP reduced porosity from 0.19 percent to 0.08 percent and the mean pore diameter from 3.2 μm to 2.8 μm, relative to the stress-relieved AM 316L.

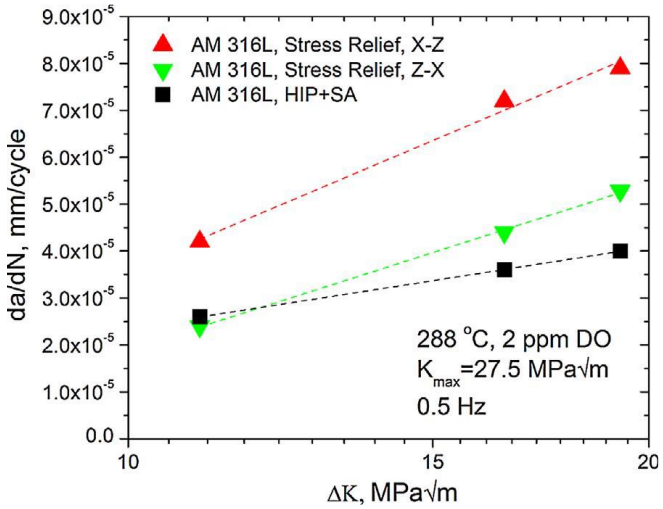

Figure 12. Corrosion fatigue crack growth rate in AM L-PBF 316L SS after stress relief in different crack orientations compared with AM 316L after HIP + SA.

The microstructure (grain structure) of AM L-PBF 316L after stress relief (650 °C for 2 h in argon), HIP (4 h at 1,150 °C and 100 MPa in argon) and recrystallization (955 °C for 4 h in argon) are displayed in Figure 13(a-c) (Lou et al. 2017).

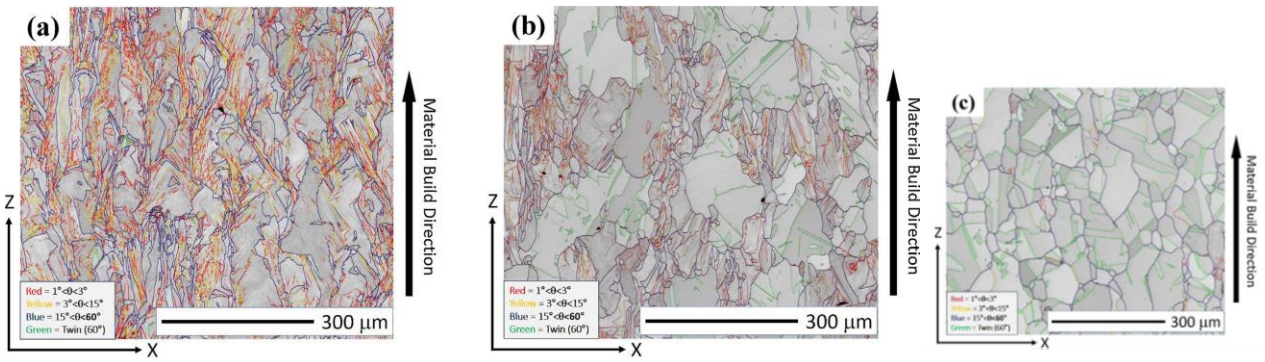

Figure 13. Electron backscatter diffraction (EBSD)-based grain structure AM LPBF 316L: (a) stress relief, 650 °C for 2 h; (b) partial recrystallization, 955 °C for 4 h; (c) HIP followed by solution annealing. “X” refers to the direction perpendicular to the material building direction, and “Z” refers to the direction parallel to the material building direction (Lou et al. 2017).

Cold-worked (CW) stainless steels are known to be susceptible to corrosion fatigue and SCC in high-temperature water typically for BWR or PWR nuclear reactor conditions (Figure 14). Cold work along the X direction results in the highest crack growth rates, while stress-relieved AM 316L SS, cold worked along the Z direction, results in similar da/dN crack propagation rates than cold-worked AM 316L SS (HIP + SA). This orientation dependency in stress-relieved material is explained by its anisotropic microstructure (Lou et al. 2017). As the load frequency decreased, the impact of environment (288 °C, 2 ppm DO) became more dominant in the corrosion process and corrosion fatigue increased significantly. At this, wrought 316L stainless steel showed lower corrosion fatigue rates than AM L-PBF after being stress relieved and after HIP and SA. Especially at low load frequencies of 10 mHz–1 mHz crack growth rates of stress relieved AM L-PBF 316L are more than twice the crack growth rates measured in wrought 316L SS at a lower stress intensity of 8.3 MPa√m.

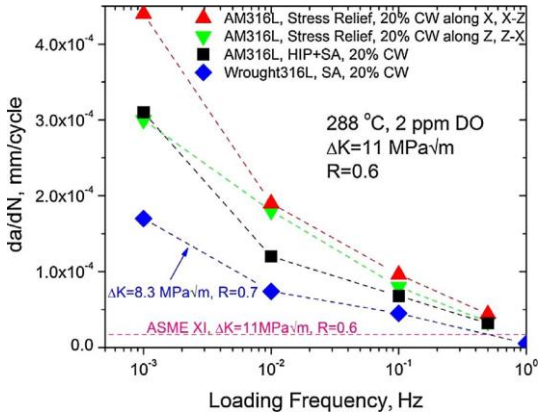

Figure 14. Corrosion fatigue crack growth rates of AM 316L with different heat treatments and crack orientations vs. wrought 316L at 288 °C (2 ppm DO) with different loading frequencies. All materials were cold worked to 20 percent (Lou et al. 2017).

3.1.5 Impact of Microstructure on AM Corrosion Properties

The microstructure and corrosion resistance of 316 L SS samples prepared using SLM and laser metal deposition (LMD) were compared with those of wrought material by Revilla et al. (2020). Different manufacturing conditions produced materials of different microstructures but fairly similar corrosion potential and passive current density values. The passivation potentials of the materials, however, show variations in the order SLM > LMD > Wrought. Therefore, AM SLM 316L showed the highest (more noble) passivation potential associated with its finer microstructure, which leads to a more stable protective oxide (Revilla et al. 2020) (Figure 15 and Figure 16).

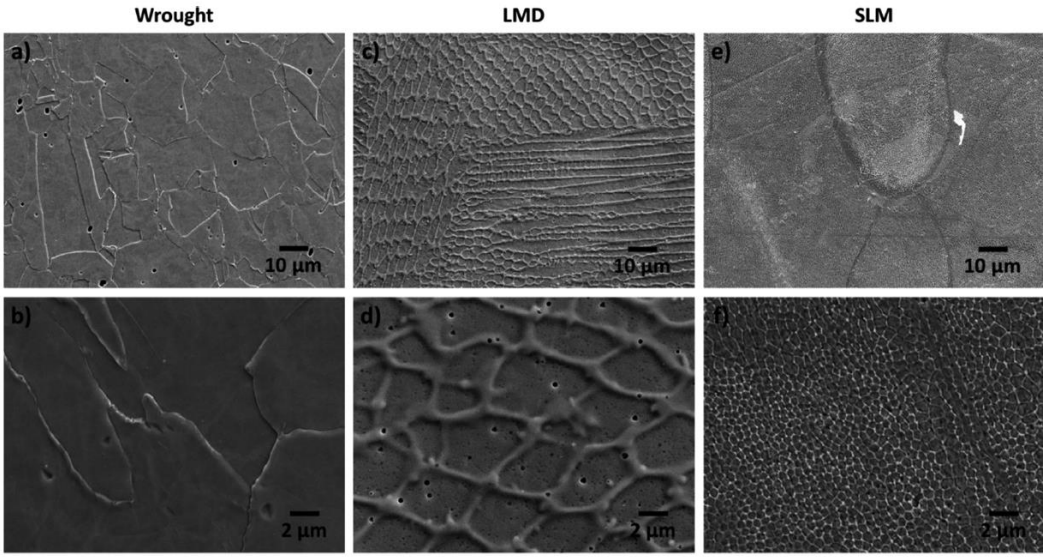

Figure 15. Microstructures of the wrought (a,b) and additive manufactured 316 L SS prepared using LMD (c,d) and SLM (e,f). The top micrographs were taken at lower magnification while the bottom micrographs were acquired at higher magnification.

During fabrication, SLM created smaller melt pools and produced much finer cellular microstructures than LMD. This affects the corrosion properties of AM 316L fabricated by different methods. The mean grain size of wrought 316L is with about 20–30 μm coarser than the cell sizes in the microstructures of LMD 316L and SLM 316L—about 4 μm and 0.7 μm, respectively. This has little impact on the corrosion potentials but strongly affects their passivation potentials, the potential the electrochemical system drives the materials to the unwanted transpassive region (Figure 16). The passivation region, defined here as breakdown potential minus the corrosion potential, was measured at 499 (±2) mV for wrought 316L and 571 (±26) mV for LMD 316L as well as 1,155 (±66) mV for SLM 316L (Revilla et al. 2020). This implies that with finer microstructures the passivation surface layer of stainless steel was maintained at far higher potentials until the passivation layer breaks down and the system becomes transpassive.

The cellular microstructure of AM 316L has a non-equilibrium nature and shows enrichments of mostly all alloying constituents—Cr, Ni, Mo, Mn, and Si—at the microstructure cell wall, while the cell center, as a result is incomplete solutionizing, is enriched with iron. We can therefore assume galvanic coupling occurs between iron in the cell center and the more noble cell wall. Iron might act as sacrificial anode, electrochemically protecting the more noble cell wall with relative higher concentrations of Cr, Ni, Mo, Mn, and Si. Without SA, the corrosion of iron in AM 316L will be therefore enhanced.

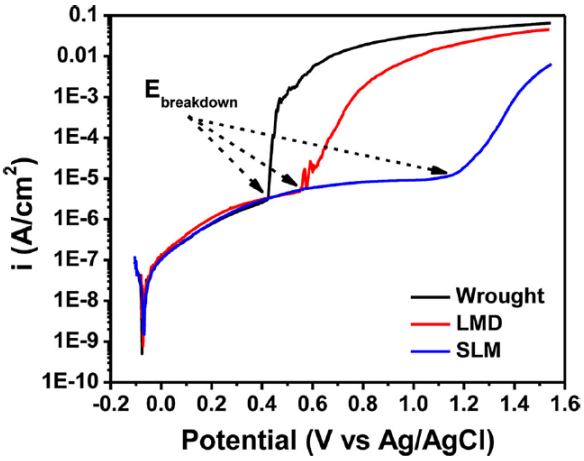

Figure 16. Potentiodynamic polarization curves of wrought 316L, LMD 316L, and SLM 316 L in 3.5 wt% NaCl (Revilla et al. 2020).

3.2 Impact of Surface Phenomena on AM Corrosion Properties

The surface roughness (R_a) of alloys produced through AM is typically high. R_a values of design parts produced through SLM are in the range of 10 μm to 30 μm (Sander et al. 2018), and therefore are about one order in magnitude larger than the R_a of parts produced by conventional manufacturing, e.g., by milling (0.8 μm), honing (0.1 μm), or lapping (0.05 μm). However, AM manufacturing parameters do affect R_a, and an increase in energy density (ϖ) can improve surface properties by reducing sporadic lack of melting, while excessive power densities can lead to formation of metallic droplets and to balling, which will again deplete surface properties.

Surface roughness is considered a defect of parts and designs fabricated by L-PBF. It is affected by the different variables that influence the manufacturing process such as the hatch distance or the energy stability of the laser used.

The effect of surface roughness on the corrosion behavior of 316 L SS manufactured by LPBF was studied by Bedmar et al. (2022). In their study, the behavior of as-built LPBF 316L was compared to L-PBF 316L after surface grinding with 2,500 grit (7–8 μm) paper. Surface treatment with 2,500 grit paper lowered the surface roughness R_a from 2.8 (±0.6) μm to 0.07 (±0.04) μm. Three different corrosion environments were used: 3.5 wt% NaCl water solution, 3 wt% H_2SO_4 solution (Figure 16), and high-temperature oxidation at 800 ºC. The surface-treated specimens, because of improved passivation layers, showed higher corrosion resistance, while in electrochemical tests the as-built L-PBF 316L showed less corrosion resistance. In high-temperature oxidation experiments, the lowest mass gain was found in the surface-treated specimens (Bedmar et al. 2022).

Decreasing the surface roughness of AM L-PBF 316L has a significant impact on the electrochemical behavior and therefore on the material's corrosion properties. Reducing the surface roughness from 2.8 μm to 0.07 μm reduces corrosion current densities and shifts the corrosion potential in the positive (more noble) direction. Under these conditions, the corrosion current densities could be reduced after surface grinding from 105 μA cm^{-2} to 17.3 μA cm^{-2} and from 52 μA cm^{-2} to 10 μA cm^{-2} for the samples immersed in 3.5 wt% NaCl for 1 h and for 360 h, respectively, while also increasing corrosion potentials from -0.98 V to -0.75 V/Ag/AgCl and from -0.99 V to -0.79 V/Ag/AgCl) after 1 h and 360 h in 3.5 wt% NaCl, respectively (Figure 17).

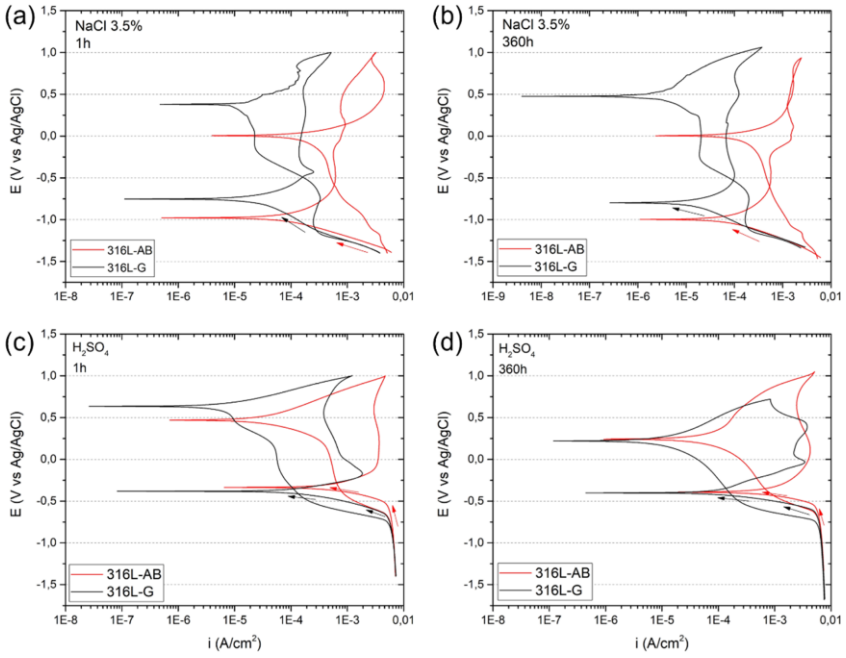

Figure 17. Cyclic potentiodynamic polarization curves of as-print 316 L-AB and surface ground 316 L-G at (a) 1 h and (b) 360 h of immersion in 3.5 wt% NaCl; and (c) 1 h and (d) 360 h of immersion in 3 wt% H_2SO_4 (Bedmar et al. 2020).

3.3 Conclusions

Concluding the following from the literature survey:

- Besides similar corrosion potentials, SLM 316L shows higher (more noble) pitting potential than wrought SS316L, and the corrosion current densities are higher than that of wrought counterparts.
- High dislocation densities lead to the lower (less noble) corrosion potentials of L-PBF 316L and lower passivation current densities. Low dislocation densities (low print speed) enable more noble corrosion potentials but larger passivation current densities.
- The impact toughness of AM 316L decreases as the oxygen level and the formation of Mn-, Mo-, or Si-oxides increase.
- Silicon-rich oxide inclusions in AM 316L reduces impact toughness and SCC properties in high-temperature water relevant to nuclear technology. Wrought 316L stainless steel shows lower corrosion fatigue rates than AM L-PBF after stress relief and after HIP and solution annealing.
- AM SLM 316L shows higher passivation potential with finer microstructural features, which leads to a more stable protective oxide passivation layer.
- Decreasing the surface roughness of AM L-PBF 316L has a significant impact its electrochemical behavior. Reducing the surface roughness reduces corrosion current densities, shifts corrosion potential in the positive (more noble) direction, and lower corrosion rates are measured.

4.0 Experimental Capabilities Needed for Corrosion Research on AM 316L Corrosion Capabilities at PNNL

The corrosion behavior of AM components and alloys is complex due to the simultaneous interaction of variables such as processing history, microstructure, corrosive environment, and temperature. Each of these factors contributes to corrosion damage at multiple length scales. The following paragraphs focus on the combination of multimodal corrosion with multiscale imaging to not only probe the corrosion behavior of these alloys but also predict the corrosion behavior using advanced computational tools spanning length scales as indicated in Figure 18 below. Employing this approach correlatively over multiple length scales has aided in the identification of microstructural features that contribute to local and global corrosion damage. This approach is particularly beneficial to the study of complex heterogeneous microstructures such as varying grain size, chemical composition, porosity, nature of oxide film. Table 1 lists all the capabilities, and the supporting capabilities are listed in the paragraphs that follow.

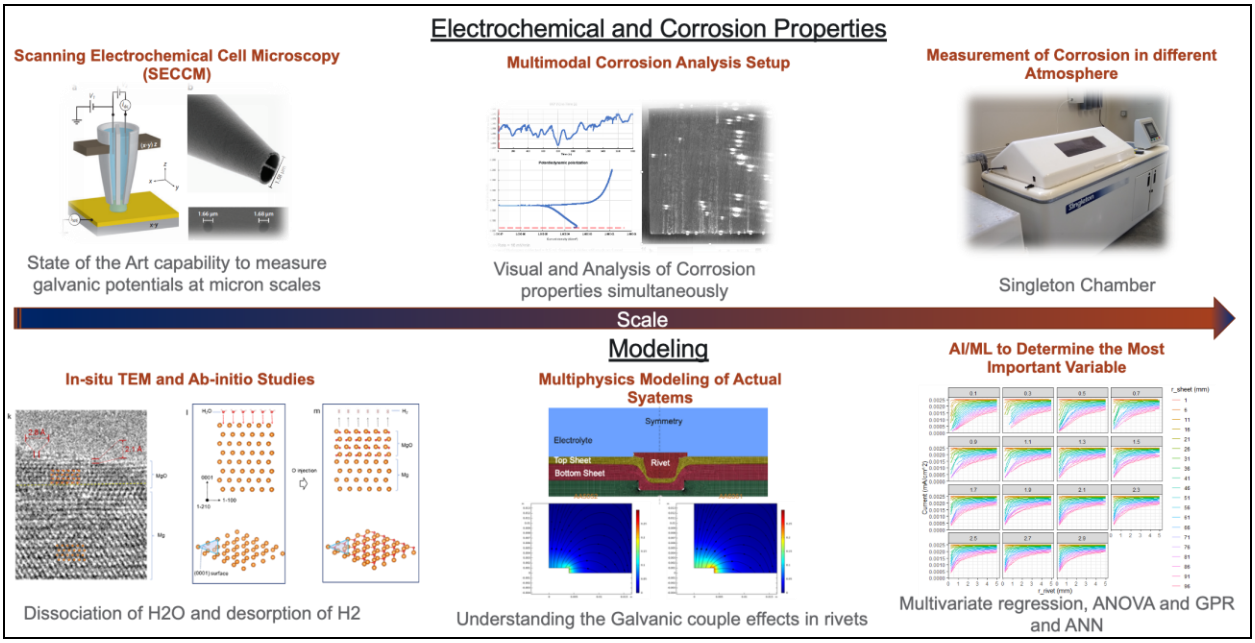

Figure 18. Determination of corrosion properties across the length scales and predictive modeling.

Table 1. Capabilities to measure corrosion at PNNL across length scales.

Facility Name	Type of Experiments	Appreciable Reactor Types	Materials Focused on
Corrosion Lab	Multimodal corrosion setup, Stress-induced corrosion tests	LWRs, BWRs, SFRs	SS, Al, steel (automotive, Naval steels), joints and interfaces, Boehmited & coated surfaces

Facility Name	Type of Experiments	Appreciable Reactor Types	Materials Focused on
Mechanical Test Lab	Thermal and fatigue stress corrosion	LWRs, BWRs, SFRs	Coatings and joint interfaces
Rad- Test Lab and 318	High-temperature aqueous corrosion testing in autoclave and ultra-high dose gamma testing.		SS, Al, Mg, U-Mo, U-Nb
Corrosion Lab	Environmental chambers – long-term storage of materials		SS, Al, steel (Automotive, Naval Steels), joints and interfaces, Boehmited and coated surfaces
ESC	Scanning electrochemical cell microscopy (SECCM)		Variety of materials capable of measuring electrochemical properties at fine scales
EMSL	Scanning Kelvin probe force microscopy		Variety of materials capable of measuring surface work function at fine scales
AMM Group	COMSOL modeling		Predicting corrosion at interfaces
AMM Group	Coating adhesion tests		Coated surfaces over structural materials

4.1.1 Corrosion Measurement Capabilities

4.1.1.1 Understanding Localized Corrosion (<10 mm and wide area mapping) on Metal Surfaces Using Scanning Electrochemical Cell Impedance Microscopy

Understanding the electrochemical properties at a localized scale is critically important to comprehending the origin of corrosion and developing multifunctional materials with robust corrosion resistance. Scanning electrochemical cell microscopy (SECCM) (Figure 19) is an emerging technique that enables the study of the corrosion of metal surfaces to be visualized at the microscopic level. At PNNL we have developed scanning electrochemical cell impedance microscopy (SECCIM) by combining SECCM with electrochemical impedance spectroscopy (EIS) and explored the unique advantages of using SECCIM to measure the corrosion kinetics on variety of materials systems and surfaces using direct current and alternating current polarization techniques. In a typical SECCIM measurement, the capillary probe filled with electrolyte and the Reference Electrode/Counter Electrode is moved down toward the sample and the tip movement stops as soon as the meniscus at the end of the capillary probe contacts the working electrode (WE) and thereby completes the electrochemical cell circuit for performing measurements. The combination of traditional SECCM with EIS led to the development of SECCIM and enabled us to study small interfacial events such as charge transfer, adsorption, and emergence of resistive

oxide films on the surface using the distribution of relaxation time analysis. Furthermore, by comparing localized SECCIM measurements with bulk electrochemical measurements, we established the reliability of SECCIM for the mapping of corrosion potential and associated charge-transfer resistance on variety of surfaces and interfaces. SECCIM measurement with Tafel and EIS analysis will provide an unparalleled ability to characterize the pitting corrosion mechanism on the heterogeneous surface of mixed-metal alloys and interfaces.

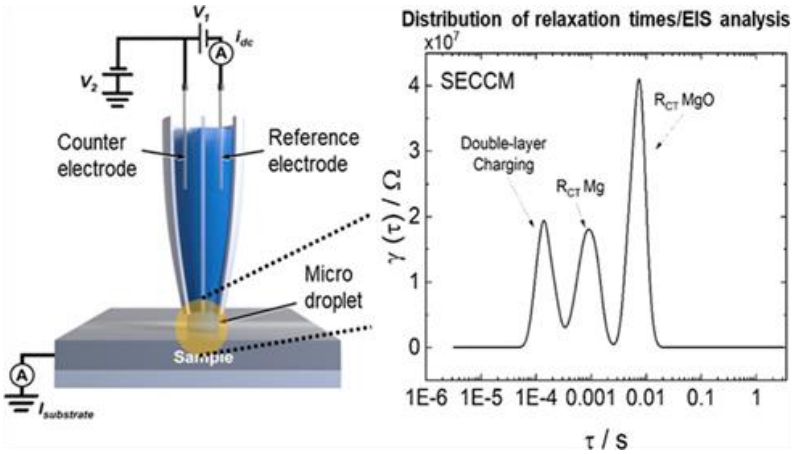

Figure 19. SECCM and SECCIM setup with Distribution of relaxation times (DRT) analysis.

Developing strategies to prevent corrosion at the interface of AM materials is challenging because of the presence of heterogeneous distribution of micro-galvanic couples and microstructural features that significantly change the corrosion rate. Devising strategies to mitigate this interfacial corrosion requires quantitative and correlative understanding of its surface electrochemical reaction. Both SECCM and SECCIM can be used to perform correlative mapping of the local electrochemical impedance spectroscopic and potentiodynamic polarization to measure the effect of electronic and microstructural changes in the AM interfacial region on corrosion kinetics. Microstructural characterization including SEM and EBSD can be performed prior to these measurements to correlate changes in microstructural features and chemistry with the corresponding electronic properties that affect corrosion behavior, as described in the paper by Prabhakaran et.al. (2023) and as shown in Figure 20. The variations in corrosion potential, corrosion current density, and EIS behavior across the interfaces or region of interest provide deeper insights into the interfacial region—which is chemically and microstructurally distinct from the bulk area and can help develop strategies that can help prevent corrosion in dissimilar metal structures.

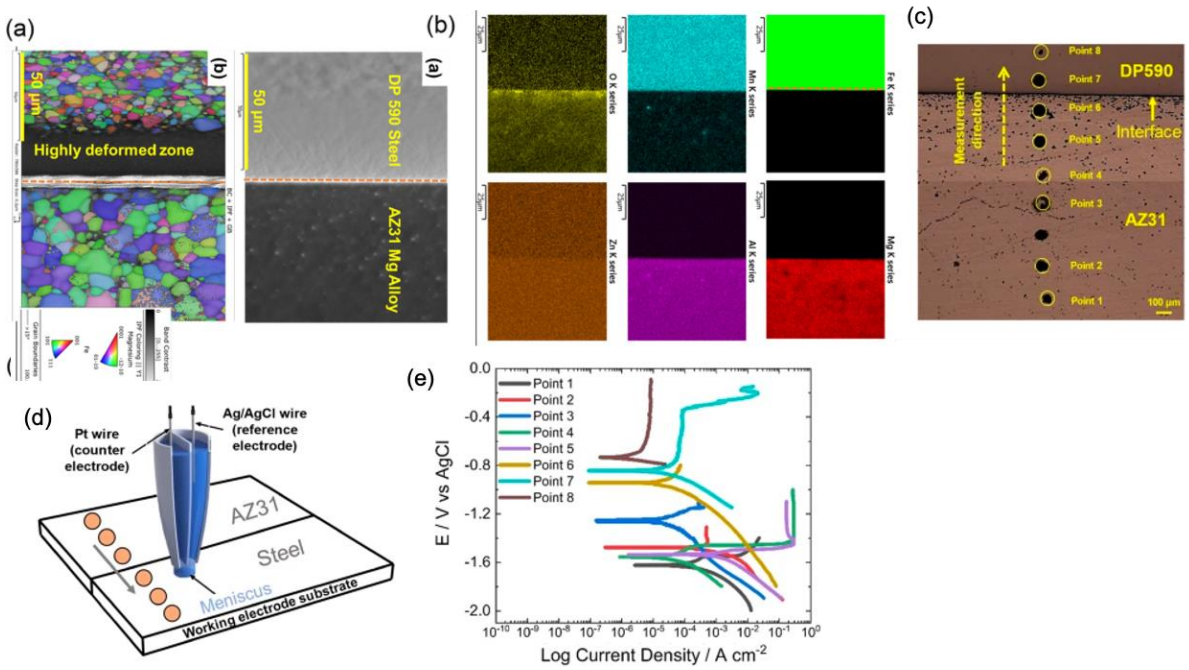

Figure 20. (a) SEM microstructure and EBSD map of friction stir welded AZ31-DP590 steel. (b) EDS maps of region used in area scan measurement. (c) Cross-sectional image of Mg-steel joint sample image after SECCIM analysis; yellow circled areas are measurement "footprints" to indicate where the SECCM/SECCIM measurements were performed. (d) Schematic of SECCM/SECCIM setup used in this study. (e) Tafel plots for the corresponding points.

4.1.1.2 In Situ Electrochemical-Atomic Force Microscopy (~100 mm² area analysis)

In situ atomic force microscopy (AFM), has been widely used to study processes at solid–liquid interfaces due to its high spatial resolution as well as its easily changeable solution parameters. In situ electrochemical AFM (EC-AFM) enables in situ investigation of topographical changes in a sample surface under different electrochemical biases controlled by a potentiostat. In situ EC-AFM experiments are performed with a Nanoscope 8 AFM (J scanner, Bruker) at room temperature (~25 °C). In situ EC-AFM capability for tracking the lateral and vertical dissolution rates of pits both at GBs and in grains with different orientations can now be extended to understanding corrosion of other commercial stainless steels and metal alloys. In addition, the ability to directly correlate EBSD with in situ AFM studies and ex situ transmission electron microscopy analysis can provide in-depth analysis of orientation dependence on the pitting corrosion of materials. Understanding such quantitative in situ studies with corrosion kinetic models can be pivotal in enhancing the predictive design of corrosion-resistant metal alloys in the future.

4.1.1.3 Bulk Electrochemical Properties Testing as per the ASTM Standard

Electrochemical testing can be performed on representative samples in different environments from 0–90°C. Anodic potentiodynamic polarization testing is conducted using a standard three-electrode setup, with the sample acting as the working electrode while two graphite rods are used

as the counter electrodes. A saturated calomel reference electrode was used for testing performed at room temperature, while an Ag/AgCl reference electrode was used for limited testing at 90 ºC. Prior to testing, the equipment performance is always verified in accordance with ASTM G5; a representative example of this verification test is shown in Figure 21. Bulk-scale potentiodynamic polarization tests can be performed in accordance with the ASTM G5 (or as recommended by the client) standards in different solutions and along with-it impedance spectroscopy can also be performed to evaluate the oxide layer resistance and stability. The open circuit potential and potentiodynamic curves polarization tests can also be performed in different pH environments using buffer solutions to understand its sole anodic and cathodic response.

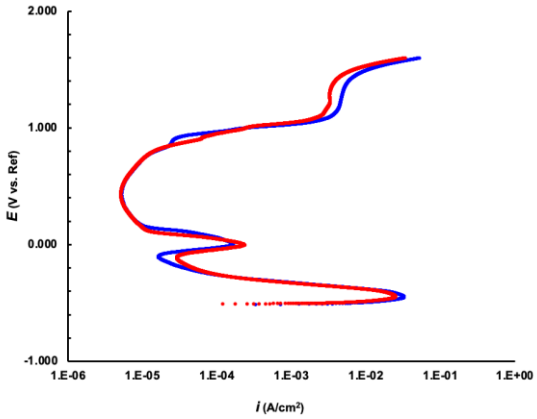

Figure 21. Representative plot for the verification of the electrochemical test setup used; blue curve illustrates ASTM G5 reference curve, red curve illustrates 430 SS sample tested.

4.1.1.4 Macro Scale Potentiodynamic Curve Using Multimodal Corrosion System

Quantitative corrosion techniques such as potentiodynamic polarization yield valuable information such as corrosion current, Ecorr, and pitting potential. However, interpreting the output from these methods can pose challenges due to the lack of precise information about how the microstructure is evolving *during* the corrosion process. Materials with significant microstructural heterogeneity (varying grain sizes or phase distribution, functionally gradient structures, etc.) can be particularly challenging to study without information about where the corrosion initiates and how it propagates on the surface. The multimodal corrosion measurement setup alleviates this challenge by bringing together multiple modalities to comprehensively study the sequence of steps involved *during* the corrosion process. Furthermore, this technique is agnostic to sample size, sample geometry and prior knowledge of material. It can also be scaled to include more measurements (e.g., pH and conductivity) and to measure corrosion in multiple samples within the same bath. In this document, we use corrosion of four alloys as examples to study fundamental corrosion processes such as passive film formation, film dissolution, pit initiation, filiform corrosion, and accompanying hydrogen release. We also show that hydrogen release rate can be an excellent qualitative indicator of localized corrosion rate. By combining these modalities, it is possible to obtain significantly more insight into corrosion processes than is possible with either one of these techniques alone. Moreover, it can be used to make an informed decision about aspects of the microstructure that can be studied in greater detail following the macroscopic corrosion process.

The sample, counter electrodes (graphite rods in Figure 22), and the reference electrode (saturated calomel electrode [SCE] in all these studies) are connected to an external potentiostat that can monitor the corrosion process as well as accelerate corrosion to gain valuable information such as corrosion current, potential etc. The system is also capable of tracking pH changes and conductivity measurements using pH and conductivity probes, respectively. We can perform open circuit potential (OCP) and potentiodynamic polarization (PD) scans in sequence to delineate the microstructural evolution in real time during the different stages of the PD curve or during long-term corrosion experiments performed for durations ranging from 24 to 150 hours. Figure 23 shows the use of a multimodal corrosion setup to visualize the degradation of the surface of steel during the potentiodynamic polarization scans. Similar studies have been performed for long-term corrosion of magnesium and steel samples.

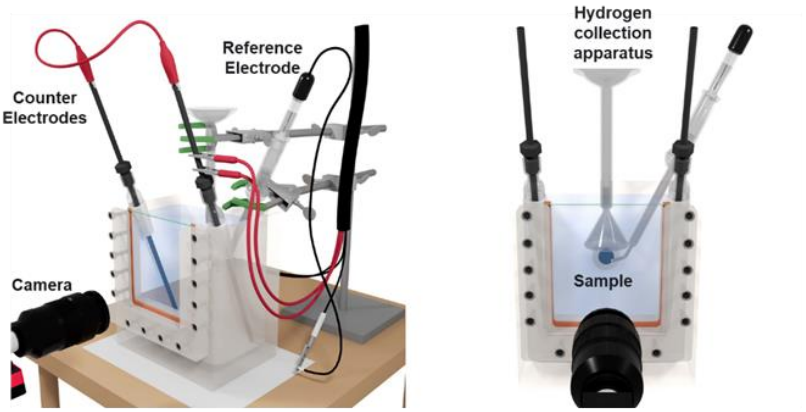

Figure 22. Schematics showing the multimodal corrosion system side view and front view.

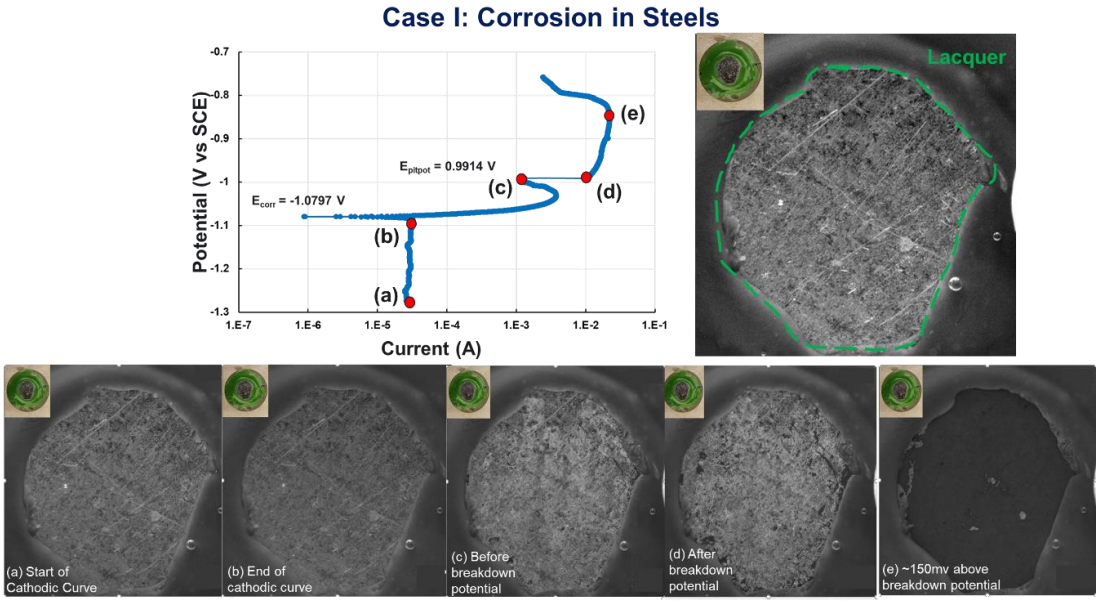

Figure 23. Use of the multimodal corrosion setup to visualize the degradation of surface of steel during the potentiodynamic polarization scans.

4.1.1.5 Exposure Testing

Exposure testing of samples in different reactor environments or solutions can be performed using the equipment at PNNL. The system consists principally of (1) a high- pressure/

temperature-capable flow-through loop consisting of a 3.8 L (nominal) autoclave, heaters, low- and high-pressure pumps to provide continual solution recirculation; and (2) a mixing loop with conductivity monitoring and control, a mixed resin demineralizer capable of producing Type I DI water or other controlled chemistry, and solution injection capabilities. All wetted portions of the system used during exposure testing are 316 stainless steel, Nitronic 50, polytetrafluoroethylene, or borosilicate glass. All wetted metallic portions of the system were previously extensively passivated and are not expected to prove particularly reactive to the dilute acids used during exposure testing. A block diagram of the system, as typically configured for use in simulated light water reactor SCC research, is shown in Figure 24.

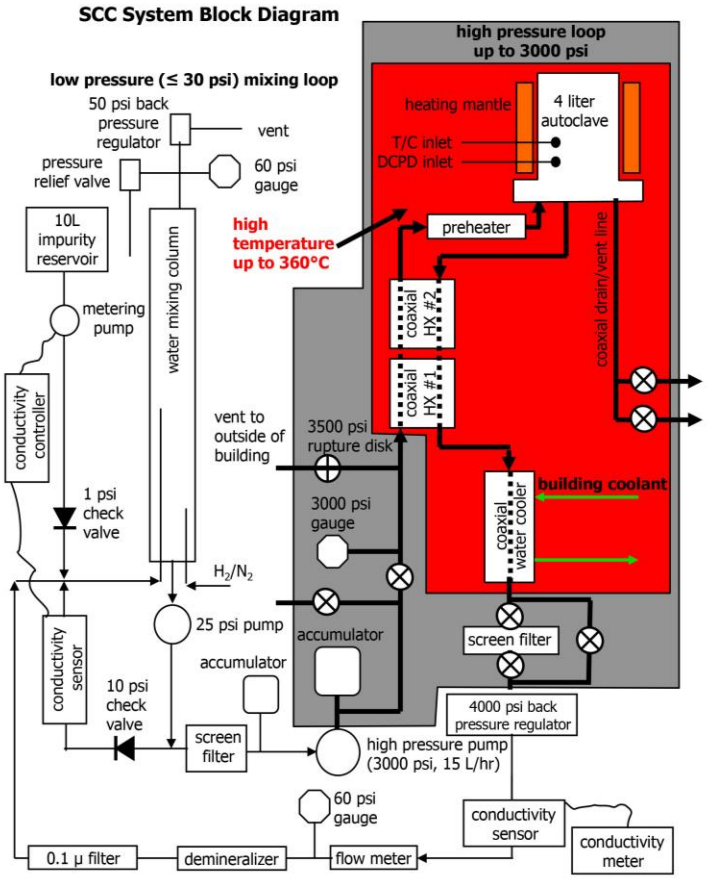

Figure 24. Block diagram of a light water reactor SCC test system used in exposure testing, showing the simulated PWR testing configuration. Courtesy of PNNL SCC Team.

Exposure testing can be conducted at temperatures from 25 ºC or 180 ºC (±1ºC) in an environment with varying pH, achieved through addition of acetic, nitric, or sulfuric acid to Type I deionized water, using pHSC4 software developed by Duke Power Company to calculate the approximate per-species concentration needed to achieve the desired pH. System pressure can be

maintained (e.g., 35 psig for 110 ºC tests, and 160 psig for the 180 ºC test). The autoclave temperature can be maintained at the target temperature ±1 ºC for the duration of each exposure. System flow can also be maintained at 150–175 cc/min for all tests, equating to approximately 2.5 autoclave exchanges per hour.

Specimens are typically suspended from a holder hanging within the autoclave; an example of the rigging used is shown in Figure 25. All rigging hardware comprised 316 SS or alloy 600. transformed, toughened zirconia (TTZ) ceramic insulators are used to prevent contact and potential galvanic coupling between the specimens and the rigging hardware. The existing platinum instrumentation wire within the test system can be considered inert to the test environment but was nonetheless routed to prevent inadvertent contact with and damage to the specimens.

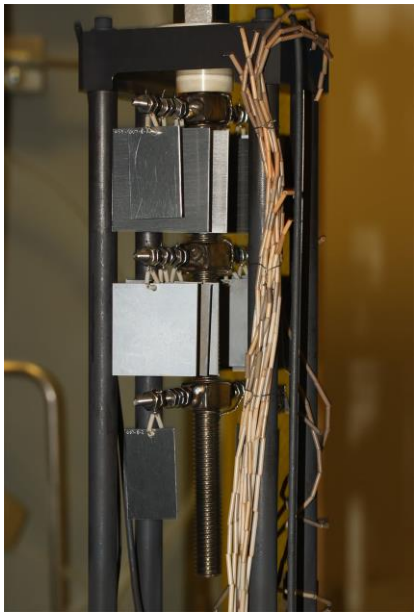

Figure 25. Example of specimen rigging in the test system prior to exposure.

4.1.1.6 COMSOL Modeling

The COMSOL multiphysics modeling tool has been used to predict the corrosion rate in joint interfaces and microstructural features/phases that can increase the corrosion rate. A computer-based corrosion modeling using a commercial software (COMSOL) with modified user code is used for this work. This tool is important to not only understand the geometrical effects on corrosion such as anode to cathode ratios but also to determine the effect of microstructure and its features on the rate of corrosion. This tool helps with validation and prediction of the experimental observations made and provides a solution to mitigate corrosion in these systems. Using this tool, the models can successfully do the following:

- Determine the initiation sites and correlate them with the characterization tasks.
- Incorporate intermetallics into the simulations.
- Develop models to predict the progression of corrosion.

The modeling also can be targeted to predict corrosion initiation sites in the material combinations and joint geometries. Further, a numerical modeling can be expanded to predict the corrosion rates in different corrosion environments and guide structural design to minimize galvanic corrosion of multiple joints in practical part-level structures.

A COMSOL model with modified user code in this work was developed to simulate galvanic corrosion of Mg in bare steel mating and cathode configuration and calculated the estimated corrosion and electrolyte potentials. Using the calculated parameters, the corrosion volume loss of Mg in the joint was modeled with increasing time. The higher corrosion depth at the bottom of Mg surface is explained by the fact that electrolyte potential is highest at the bottom of the exposed Mg surface (shown in Figure 26a). As the current leaving the anode flows toward the cathode, the potential must be the highest at the bottom of the Mg bar. Therefore, the overpotential (and therefore the corrosion rate) is highest at the end of the bar.

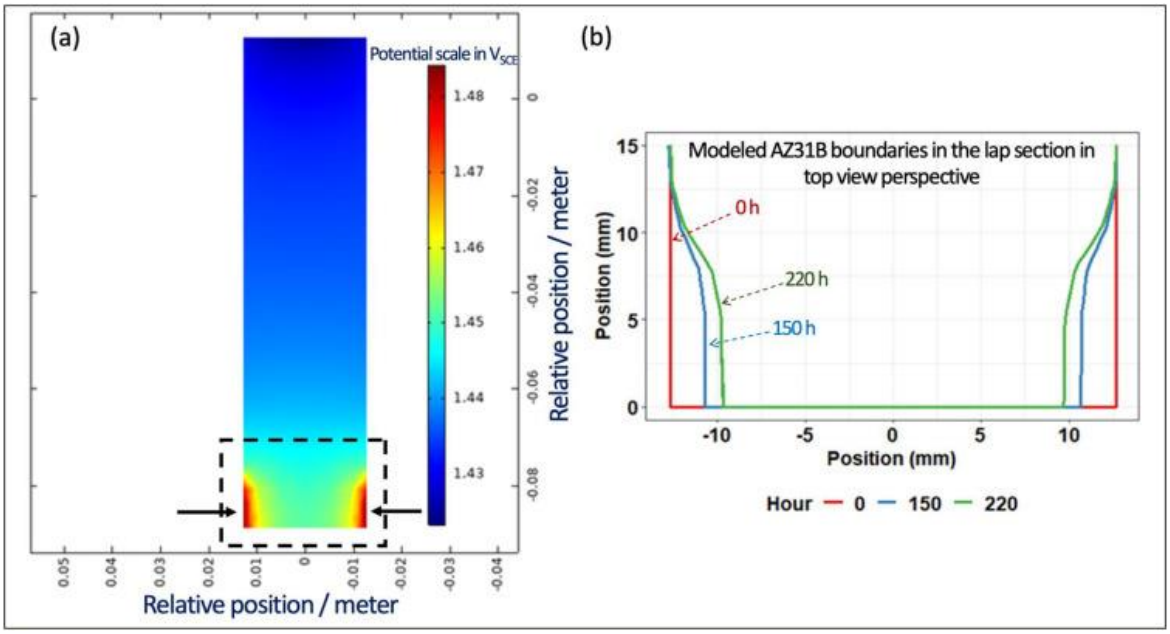

Figure 26. (a) COMSOL-modeled electrolyte potential map over Mg bar plotted in line with a potential distribution theory Prabhakaran et.al. (2023). Electrolyte near the anode (dotted black box with black arrows) presents more positive potential. (b) Prediction of Mg volume loss over time plotted in a top view of the AZ31B bar.

4.1.1.7 Modeling the Role of Anodic and Cathodic Particles on the Corrosion Behavior of Alloys

In most alloys, the microstructure consists of anodic and cathodic particles and their size/spacing distribution depends on different thermomechanical heat treatment processes. Fragmentation and rearrangement of these phases along with generation of different defects like vacancies, dislocation, and twins have been observed to degrade the corrosion resistance of the alloy. However, a lot of conflicting hypotheses and observations have been made in the literature and this ambiguity arises from the presence and interdependence of a number of factors like grain size, texture, defect density due to deformation, second phase particle size, and their distribution in the matrix. Therefore, it is highly important to understand the individual effect of each

parameter as well as their interdependence to design future generations of alloys. At PNNL we have developed a finite element-based numerical framework/multiphysics approach that can help deconvolute the effect of the size and distribution of cathodic and anodic intermetallic phases on localized corrosion behavior. In Figure 27, a single cathodic intermetallic phase was disintegrated into several smaller particles keeping the overall cathodic surface area, hence cathode to anode ratio, constant to observe the effect of fragmentation on the current density of the system. Additionally, the spatial distribution of fragmented particles was varied by changing the radial separation distance between them to observe the effect of distribution on the localized corrosion behavior of the Mg alloy. The results of this study, we significantly improved the corrosion resistance of the magnesium alloy (Beura, V. et. al., 2022), (Niverty, S. et. al., 2023) (Venkateshkumar, P. et. al., 2022). Coupled with SECCM and AFM techniques one can easily determine the potential of these phases, and the multi modal corrosion (MMC) setup can validate the corrosion rate in these alloys.

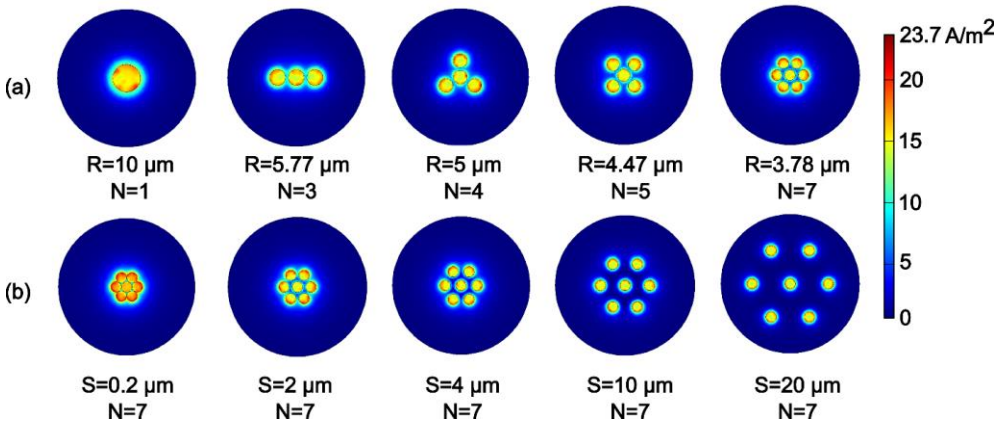

Figure 27. Effect of cathodic particle distribution on the magnitude of electrolyte current density. (a) Fragmentation of a single cathodic β phase into a different number of particles (N) with different sizes (R), keeping the overall anode to cathode ratio constant. (b) Change in anodic current density with increasing separation distance (S) between multiple fragmentations (N=7) of cathodic particles of same radius.

4.1.1.8 Understanding Mechanistic Pathways Using Atomistic Modeling/Density-Functional Theory

Understanding the mechanistic pathways of reaction of different solutions with the underlying metal surface is highly critical. Earlier work by the authors used this approach to guide the experimental work to identify surface design strategies to reveal the mechanisms and energetics of H_2O reactions with doped Mg surfaces and to quantify the stability of the reaction products. This type of modeling provided improved fundamental understanding of surface chemistry/ corrosion behavior relationships. These simulations helped identify the surface sites most vulnerable to H_2O attack established which dopants provide the best protection against it. Computational study using density-functional theory (DFT) was performed on the Mg surfaces using different dopants, such as Al, Mn, Zn, and Ce. The processes, such as H_2O adsorption, dissociation on these surfaces, and the surface oxidation, were investigated. The interactions of Cl- with surface compositions such as MgO, $MgCO_3$, $Mg(OH)_2$, Al_2O_3 and $MgAl_2O_4$ were investigated using DFT.

5.0 Suggested Path Forward for the corrosion work on the AMMT Program

The literature survey revealed that no significant database or history exists for the corrosion behavior of AM products, including no good comparative benchmark study between different additive manufacturing techniques. The limited corrosion experimental evaluations showed a potential for improved corrosion resistance of 316L materials. However, the effect of composition microstructure and corrosion seems not to be explored and is recommended for future work.

As fabricated, net shape AM components can be further beneficial because surface roughness reduces corrosion current densities, shifts corrosion potential in the positive (more noble) direction, and lowers corrosion rates. These needs to be quantified for the different AM techniques and specifically in relation to the residual stresses and microstructures.

Corrosion ***mechanistic*** studies seem not to be explored significantly and are highly recommended as an important focus of future work. Such studies can be performed using modeling and experiment in concert. The capability and available facilities at PNNL provide a base for future experimental work and modeling for corrosion mechanistic studies. Specifically, understanding the mechanistic pathways of the reaction of different solutions with the underlying metal surface is highly critical. Earlier work by the authors used this approach to guide the experimental work to identify surface design strategies to reveal the mechanisms and energetics. The results of this type of modeling improved fundamental understanding of surface chemistry/corrosion behavior relationships and these simulations can help identify the surface sites most vulnerable to specific species attack as well as establish which grain/chemical composition/microstructure provide best the protection against it.

Finally, it is recommended that a complete PIRT analysis be performed for each reactor type to fully comprehend the corrosion and other environmental challenges. This will ensure that the AMMT program is developing a corrosion strategy focused on application and can therefore provide the methodologies for future application of measures for a variety of material types.

6.0 References

Bedmar, J., Abu-warda, N., García-Rodríguez, S., Torres, B., Rams, J. 2022. Influence of the surface state on the corrosion behavior of the 316 L stainless steel manufactured by laser powder bed fusion. *Corrosion Science* 207, 110550.

Beura, V., Zhang, D., Overman, N., Darsell, J., Herling, D.R., Solanki, K., Joshi, V.V., 2022, Enhanced mechanical behavior and corrosion resistance of AZ31 magnesium alloy through a novel solid-phase processing, *Corrosion Science* 197, 110074

Jokisaari, A. 2023. Corrosion work packages. AMMT Technical Review Meeting, Chicago, May 8, 2023.

Lou, X., Andresen, P.L., Rebak, R.B. 2018. Oxide inclusions in laser additive manufactured stainless steel and their effects on impact toughness and stress corrosion cracking behavior. *Journal of Nuclear Materials* 499, 182-190.

Niverty, S., Kalsar, R., Strange, L., Prabhakaran, V., Joshi, V.V. (2023). Integrating Multimodal Corrosion with Correlative Microscopy Across Multiple Length Scales. In: Barela, S., Leonard, A., Maier, P., Neelameggham, N.R., Miller, V.M. (eds) Magnesium Technology 2023. TMS 2023. The Minerals, Metals & Materials Series. Springer, Cham. https://doi.org/10.1007/978-3-031-22645-8_15

Lou, X., Orthon, M.A., Rebak, R.B. 2017. Corrosion fatigue crack growth of laser additively-manufactured 316L stainless steel in high temperature water. *Corrosion Science* 127, 120-130.

Prabhakaran V., L. Strange, R. Kalsar, O.A. Marina, P. Upadhyay, and V.V. Joshi. 2023. Investigating electrochemical corrosion at Mg alloy-steel joint interface using scanning electrochemical cell impedance microscopy (SECCIM). *Scientific Reports* 13, 13250. https://doi.org/10.1038/s41598-023-39961-2.

Revilla, R.I., Calster, M.V., Raes, M., Arroud, G., Andreatta, F., Pyl, L., Guillaume, P., Graeve, I.D. 2020. Microstructure and corrosion behavior of 316L stainless steel prepared using different additive manufacturing methods: A comparative study bringing insights into the impact of microstructure on their passivity. *Corrosion Science* 176, 108914.

Sander, G., Tan, J., Balan, P., Gharbi, O., Feemstra, D.R., Singer, L., Thomas, S., Kelly, R.G., Scully, J.R., Birbillis, N. 2018. Corrosion of Additively Manufactured Alloys: A Review. *Corrosion* 74(12): 1318-1350.

Sander, G., Thomas, S., Cruz, V., Jurg, M., Birbilis, N., Gao, X., Brameld, M., Hutchinson, C.R. 2017. On The Corrosion and Metastable Pitting Characteristics of 316L Stainless Steel Produced by Selective Laser Melting. *Journal of The Electrochemical Society* 164(6): C250-C257.

Sprouster, D.J., Cunningham, W.S., G.P.H. a, H.Y. , P. A, Huang, X., Olds, D., Tilton, M., Chu, Y.S., Dooryhee, E., Manogharan, G., Trelewicz, J.R. 2021. Dislocation microstructure and its influence on corrosion behavior in laser additively manufactured 316L stainless steel. *Additive Manufacturing* 47, 102263.

Venkateshkumar Prabhakaran*, Rajib Kalsar, Lyndi Strange, Olga A. Marina, Ramprashad Prabhakaran, and Vineet V. Joshi* “Understanding Localized Corrosion on Metal Surfaces Using Scanning Electrochemical Cell Impedance Microscopy (SECCIM)” J. Phys. Chem. C 2022, 126, 30, 12519–1252. 2022

Pacific Northwest National Laboratory

902 Battelle Boulevard
P.O. Box 999
Richland, WA 99354
1-888-375-PNNL (7665)

www.pnnl.gov